



Advancing Remote Sensing for Health Monitoring: A Novel Framework for Precise Vital Sign Detection via IR-UWB Radar

Yizhu Wang , *Student Member, IEEE*, and Jing Liang , *Senior Member, IEEE*

Abstract—The impulse-radio ultra-wideband (IR-UWB) radar is ideally suitable for noncontact monitoring of respiratory rate and heart rate due to its noninvasive nature and high penetration capabilities. This investigation proposes a novel framework using the IR-UWB technology for remote health monitoring. It integrates expectation maximization with the grey wolf optimizer and employs advanced multivariate correlation analysis to improve the accuracy and reliability of vital sign detection. Our approach outperforms mainstream methods, such as the chirp Z-transform and moving target indicator, variational mode decomposition, and multivariate correlation method, in terms of both estimating frequencies and amplitudes. Our work demonstrates outstanding robustness and adaptation to various body orientations via real human body data collection experiments, which promotes noncontact health monitoring for human care.

Index Terms—Frequency and amplitude estimation, impulse-radio ultra-wideband (IR-UWB) radar, noncontact health monitoring, remote sensing, vital sign analytics.

I. INTRODUCTION

ADVANCES in remote sensing technology have opened new avenues for noncontact medical monitoring, promising substantial benefits to global health security [1]. Over the last decade, radar technology, specifically impulse-radio ultra-wideband (IR-UWB) radar, has stood out as a powerful tool [2], [3], [4], [5].

IR-UWB radar has exceptional noncontact vital sign monitoring capabilities, offering distinct advantages over continuous wave (CW) and frequency-modulated CW radars. Its ability to emit extremely short pulses (e.g., 0.1–2 ns) enhances power efficiency and high-range resolution [6]. Combined with its wide bandwidth, IR-UWB radar penetrates obstacles and minimizes multipath interference, making it highly effective for precise vital sign detection [7].

Traditional monitoring technologies, requiring direct body contact and often causing discomfort, are less feasible for burn

victims, highly infectious patients, infants, and individuals in postdisaster scenarios [8], [9]. IR-UWB radar, capable of penetrating clothing, offers a nonintrusive alternative. Operating at a transmission power below -41 dBm/MHz, IR-UWB facilitates discreet, continuous monitoring, ideal for environments, such as nursing homes and smart homes [10]. It enables healthcare professionals to remotely monitor patients with infectious diseases, thereby reducing the risk of infection. Given the advantages above, its applications have broadened significantly across various healthcare fields. These include specialized patient monitoring [11], sleep analysis [12], [13], vital sign detection within vehicles [14], [15], [16], [17], and emergency responses after disasters [8], [12], [18].

In recent years, researchers have introduced a range of methods for detecting vital signs with IR-UWB radars. These methods are typically classified into three primary groups: spectral analysis, periodicity-based, and blind source separation methods.

Spectral analysis is a widely used method for estimating vital signs. It converts raw signals to the frequency domain, using techniques, such as fast Fourier transform (FFT) for peak detection after preprocessing. To refine FFT's accuracy, a combination with a third-order differentiator has been shown to optimize SNR [19]. Lazaro et al. [3] enhanced frequency resolution beyond FFT by employing the chirp Z-transform (CZT) with a harmonic cancellation filter, enabling heart rate (HR) estimation in a respiration-free spectrum. Recent advancements include techniques, such as those described in [20], which explore optimized feedback notch filters for suppressing respiratory harmonics, thereby further enhancing the accuracy of HR measurements in the presence of overlapping signals. In addition, the short-time Fourier transform addresses FFT's spectral leakage, offering a time-related spectrum with short window lengths [21].

Respiratory and heartbeat signals generate periodic peaks in the time or frequency domain, whereas noise peaks appear randomly; periodicity-based methods employ this characteristic. Nguyen et al. [22] introduced the harmonic path algorithm to estimate respiratory rate (RR) and HR by identifying periodic harmonic paths. Moreover, the chest cavity's periodic motion produces regular patterns in fast- and slow-time domains. Thus, by processing signals received across multiple range bins, the signals that are masked by noise can be identified [23], [24].

Manuscript received 28 April 2024; revised 5 July 2024; accepted 3 August 2024. Date of publication 7 August 2024; date of current version 19 August 2024. This work was supported in part by the Sichuan Science and Technology Program under Grant 2023NSFSC0450 and in part by the 111 Project under Grant B17008. (Corresponding author: Jing Liang.)

The authors are with the School of Information and Communication Engineering, University of Electronic Science and Technology of China, Chengdu 611731, China (e-mail: yizhuwang@std.uestc.edu.cn; liangjing@uestc.edu.cn). Digital Object Identifier 10.1109/JSTARS.2024.3439750

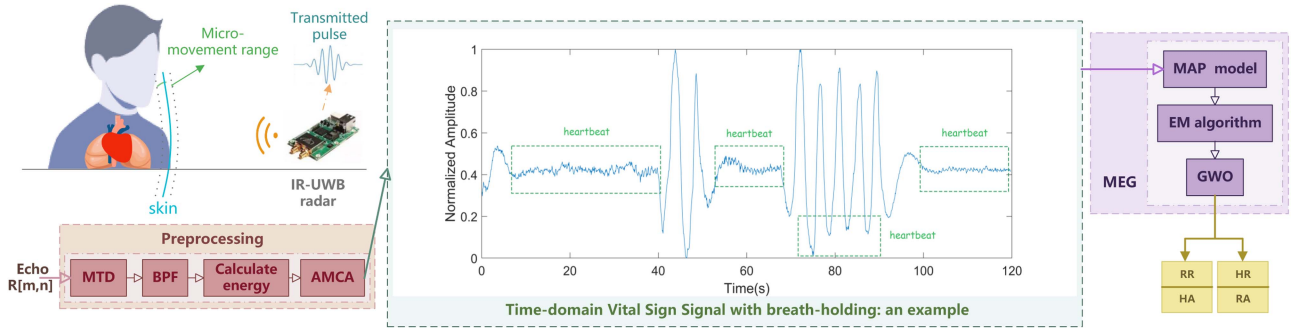


Fig. 1. Overall processing chain: Estimate the FARH using the proposed framework. The example shown in the middle of the figure is a time-domain plot of VSS during breath-holding. It is evident that within the three breath-holding intervals, fluctuations are solely caused by heartbeats. Compared to moments accompanied by breathing, the amplitude of the heartbeats is smaller, while their frequency is higher relative to breathing.

Blind source separation methods seek to decompose mixed signals and extract vital sign signals (VSS) based on various criteria. The multiple signal classification (MUSIC) method, effective even amidst motion artifacts or car vibrations, can isolate heartbeat harmonics with a fixed P value [25]. Variational mode decomposition (VMD) surpasses empirical mode decomposition (EMD) in noise resistance and sampling efficiency, enhancing its suitability for VSS extraction [24], [26], [27], [28]. Duan and Liang [5] applied VMD, extracting vital signs from the Hilbert spectrum to monitor changes in real time.

For spectral analysis and periodicity-based methods, various components, such as respiratory harmonics, and intermodulation products of RR and HR may fall within the HR band, leading to misjudgment of the HR component [29]. Although higher order heartbeat harmonics can avoid the influence of these factors, they might be too weak and are vulnerable to other noise [23], [24]. For blind source separation methods, the decomposition result relies on subjectively selected parameters, such as P for MUSIC [30], [31], WGN for EMD [32], [33], [34], and K and α for VMD [35], [36]. These parameters are empirically derived and require adjustment when the monitoring environment changes. Inappropriate parameter choices may cause modal mixing or excessive decomposition, preventing the precise extraction of vital signs.

To ensure reliable VSS, the above methods generally compare the maximum peak frequency to that detected by contact sensors. However, most lack mathematical basis or merely decompose mixed signals nonlinearly, relying on visual identification of VSS. Furthermore, in applications, such as respiration classification and sleep disorder monitoring, precisely measuring the amplitude of respiratory and heartbeat signals is equally essential [37].

In this work, we propose a novel framework based on the IR-UWB system technology for vital sign estimation. Fig. 1 illustrates the overall flowchart. The contributions are as follows.

- 1) *Establishment of a robust framework for noncontact vital sign monitoring*: The framework consists of several sub-modules. In the preprocessing stage, we propose advanced multivariate correlation analysis (AMCA) to optimize vital sign data utilization and enhance system resilience against noise and diverse human orientations. During the core processing phase, the MEG [maximum a posteriori

(MAP)–expectation maximization (EM)–grey wolf optimizer (GWO)] method is designed to utilize EM and GWO via MAP estimation, automatically extracting frequency and amplitude information from VSS.

- 2) This work is compared with prevalent benchmarks, showing notable improvements in HR estimation accuracy and advancing the precise extraction of vital signs' amplitude.
- 3) The effectiveness of the proposed framework has been validated through a combination of simulations and onsite experiments, both of which verified accuracy and adaptation to various situations.

The rest of this article is organized as follows. Section II presents the vital signs model for IR-UWB radar. Section III outlines the comprehensive framework for estimation, discussing the preprocessing stage and using the MEG method for estimating both the frequency and amplitude of respiratory and heartbeat (FARH) signals. Section IV conducts simulation experiments on continuous human monitoring and analyzes the results. Section V details the onsite experiments, and validates the proposed framework. Finally, Section VI concludes this article.

II. VITAL SIGN BASIC MODEL OF IR-UWB RADAR

Fig. 1 illustrates a typical IR-UWB radar scenario acquiring vital signs, where the radar system emits a narrow pulse signal toward the subject. The receiver captures these echoes and processes the data preliminary before storage. These data are then transferred to a personal computer via a microprocessor for further extraction of the subject's vital sign information.

The waveform emitted in this work is a Gaussian-modulated pulse, with the m th pulse iteration defined by

$$s(t) = A \exp \left[-\frac{(t - mT_s)^2}{2\sigma^2} \right] \sin [2\pi f_c(t - mT_s)] \quad (1)$$

where A denotes the amplitude of the transmitted pulse, T_s is the pulse repetition period, σ represents the standard deviation governing the pulse width, f_c is the center frequency of the transmitted pulse, and t signifies the fast time.

The human chest's movement is modeled as sinusoidal vibrations, reflecting the natural, subtle motions associated with respiration and heartbeat. These micromotions create variations

in the distance between the chest and the radar, mathematically represented by sinusoidal functions

$$d(\eta) = d_0 + A_r \sin(2\pi f_r \eta) + A_h \sin(2\pi f_h \eta) \quad (2)$$

where $d(\eta)$ denotes the time-varying distance caused by respiratory and heartbeat movements over slow time η . d_0 is the fixed distance between the transceiver antenna and the human chest. f_r and A_r are the RR and respiratory amplitude (RA), respectively. f_h and A_h are the HR and heartbeat amplitude (HA), respectively.

The corresponding time delay of this pulse is denoted by

$$\tau_d(\eta) = \frac{2d(\eta)}{c'} \quad (3)$$

where c' is the propagation speed in the air.

In real-world settings, radar signals are reflected off not just the primary target but also various objects within the room, causing multiple reflections. These can be modeled as the sum of reflections from point scatterers, each of which is characterized by its own gain and time delay. Assuming that the room contains one person and i static clutter items, all treated as point scatterers, the total reflection from any point on the target surface within the same range bin can be viewed as a collective reflection via a single propagation path [38]. The channel impulse response is given by

$$h(\eta, t) = \alpha_d \delta(t - \tau_d(\eta)) + \sum_i \alpha_i \delta(t - \tau_i) \quad (4)$$

where $\delta(\cdot)$ represents the Dirac delta function and i is the path index. α_d and τ_d denote the reflected gain and time delay of the human, respectively. Similarly, α_i and τ_i are the reflected gain and time delay of the i th static object, respectively.

The echo $r(\eta, t)$ is represented by the convolution of the transmitted pulse $s(t)$ with the channel impulse response $h(\eta, t)$, including additive system noise for completeness

$$\begin{aligned} r(\eta, t) &= s(t) * h(\eta, t) + n(\eta, t) \\ &= \alpha_d s(t - \tau_d(\eta)) + \sum_i \alpha_i s(t - \tau_i) + n(\eta, t). \end{aligned} \quad (5)$$

The collected echo is stored in a 2-D matrix, $R[m, n]$, where m and n represent the slow-time and fast-time indices, respectively

$$\begin{aligned} R[m, n] &= r[\eta = mT_s, t = nT_f] \\ &= \alpha_d s(nT_f - \tau_d(mT_s)) + \sum_i \alpha_i s(nT_f - \tau_i) \\ &\quad + n(mT_s, nT_f) \end{aligned} \quad (6)$$

where m denotes the sampling point in slow time. T_f and n denote the sampling period and the sampling point in fast time, respectively. In the IR-UWB radar system, “fast-time” components capture immediate pulse travel times for distance measurements, while “slow-time” components track these over time to monitor changes in the target’s position or state. This enables precise tracking of both static and dynamic target features, crucial for applications, such as vital sign monitoring.

III. ESTIMATING VITAL SIGN FREQUENCY AND AMPLITUDE USING THE PROPOSED FRAMEWORK

A. Preprocessing

1) *Removal of Static Clutter*: Reflected by static objects, IR-UWB echoes produce static environment clutter, as detailed in (6). This unwanted clutter requires removal. Vibrations from the human chest, caused by respiration and heartbeat, act as a moving target. By applying the moving target detection (MTD) method, we calculate the average signal amplitude across all slow-time samples for each fast-time range bin, subtracting this average from the slow-time signal for each bin. The procedure is as follows:

$$R' [m, n] = R [m, n] - \frac{1}{M} \sum_{m=1}^M R [m, n] \quad (7)$$

where M represents the total number of slow-time samples.

2) *Bandpass Filtering (BPF)*: After eliminating static environment clutter, low-frequency clutter and high-frequency noise remain. We employ (BPF with a passband range of 0.13–4 Hz to isolate the relevant components to be measured.

Fig. 2(b) illustrates an example after MTD and BPF processing, and the subsequent work is built upon these data.

The VSS is not limited to the precise distance of the individual; rather, it exists within an area influenced by the individual’s chest cross section (CCS). For an adult, the CCS typically averages around 0.4 m² [23]. Moving beyond traditional single-range bin methods, we propose the AMCA, designed to enhance SNR and better utilize vital sign information.

3) *Calculate the Energy for Each Range Bin*: Calculate the energy of the signal in each range bin separately for the preprocessed echo matrix. Each range bin signal’s energy is determined as follows:

$$E [n] = \sum_{m=1}^M |R' [m, n]|^2. \quad (8)$$

Fig. 3(a) displays the signal energy under each range bin.

4) *AMCA*: Selecting the range bin signals that satisfy the following conditions as the VSS. The threshold T_h is established using the statistical 3σ rule, specifically set to $m - \sigma$ (mean minus one standard deviation) based on extensive experimental observations

$$V := \{n \mid E[n] \geq T_h\}$$

$$T_h = \frac{1}{N} \sum_n E[n] - \sqrt{\sum_n \left(E[n] - \frac{1}{N} \sum_n E[n] \right)^2} \quad (9)$$

upon identifying the range bin that fulfills (9) and exhibits the highest energy, denoted as $n = p$, alongside the surrounding range bins ranging from $n = p - x$ to $n = p + y$, the corresponding signals from $s_{p-x}(\eta)$ to $s_{p+y}(\eta)$ are subjected to

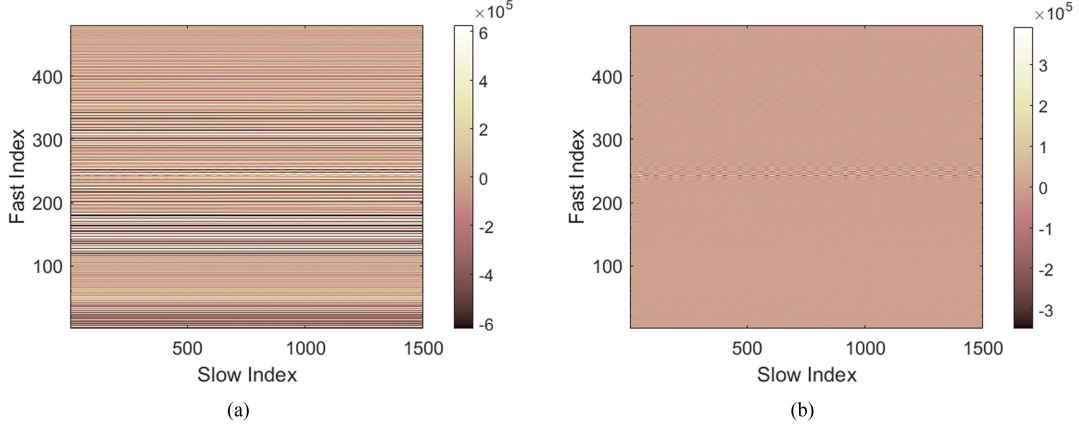


Fig. 2. Comparison of the echoes before and after applying MTD and BPF. (a) Initially, the raw echoes are reflections from the human target and static objects, compounded by system noise. (b) Human micromotion signals after eliminating static clutter. The energy from human respiration and heartbeat vibrations varies with time and position. On the slow time, respiratory and heartbeat pulsations show rhythmic periodicity. On the fast time, the energy distribution of the human form becomes discernible, with values concentrated between 220 and 260, clearly indicating the subject's position.

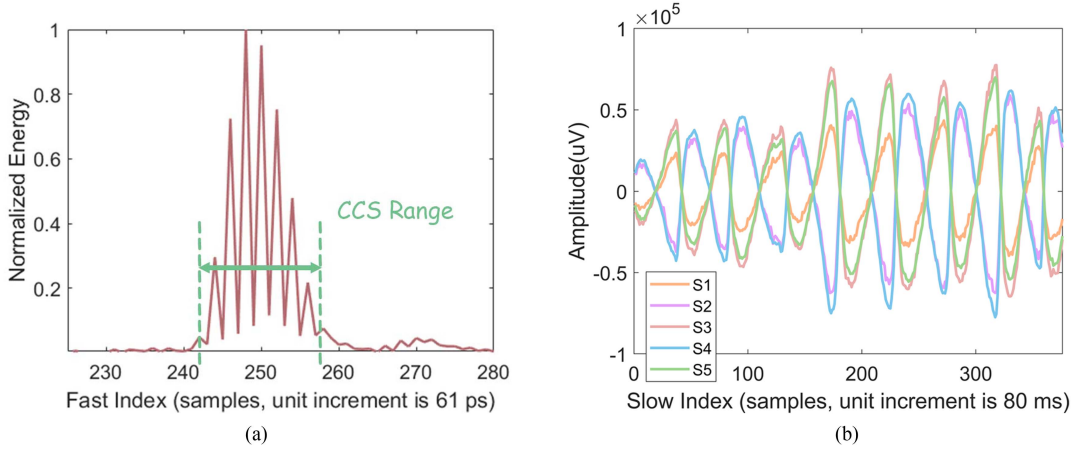


Fig. 3. Extraction of VSS at fast index. (a) Normalized energy profile at the fast index reveals that five points conform to (9). (b) Extracted VSS in the time domain. S1-S5 are all selected 1-D VSS that satisfy (9), whose consistent trends in oscillation frequency. The heartbeat vibration is nearly visible, and although its amplitude is smaller than that of respiration, its frequency is higher.

cross-correlation processing to obtain $S_c(\eta)$. Each range bin includes RR, HR, and their harmonics and intermodulation products. Cross-correlation processing removes unrelated noise, extracting and strengthening above common components. The specific expressions are as follows:

$$S_c(\eta) = \frac{1}{N} \sum_{i=-x}^y \sum_{j=-x}^y \text{corr}(s_{p+i}(\eta), s_{p+j}(\eta)) \quad (10)$$

where $s_{p+i}(\eta)$ and $s_{p+j}(\eta)$ denote the respective signals, i and j range from $-x$ to y , indicating the inclusion of the central range bin and two neighboring bins on each side. The cross-correlation function $\text{corr}(s_{p+i}(\eta), s_{p+j}(\eta))$ measures the similarity between the two time-shifted signals. N is the normalization factor that scales the output to ensure the resulting signal falls within an appropriate range of values.

Fig. 3(b) provides an example where all displayed signals are selected 1-D VSS with consistent oscillation frequencies.

B. MAP Model

The echo can be expressed as follows:

$$y = S_c(\eta) + n(\eta) = r + n \quad (11)$$

where n represents white noise, and r denotes the $S_c(\eta)$.

As demonstrated in Fig. 4, the experimental results show that both the FARH values and white noise follow normal distributions, based on a large number of samples collected.

Using $s_c(\eta)$, we construct a posteriori probabilistic model for the FARH, as outlined in the following equations:

$$\begin{aligned} p(\vec{x}|y) &= \frac{p(y|\vec{x}) \cdot p(\vec{x})}{p(y)} \\ &= \frac{\left(\frac{1}{\sqrt{2\pi\sigma^2}}\right)^N e^{-\frac{(y-r)^H(y-r)}{2\sigma^2}} \frac{1}{(2\pi)^2|\Lambda|^{1/2}} e^{-\frac{(\vec{x}-\vec{\mu})^H\Lambda^{-1}(\vec{x}-\vec{\mu})}{2}}}{\int \left(\frac{1}{\sqrt{2\pi\sigma^2}}\right)^N e^{-\frac{(y-r)^H(y-r)}{2\sigma^2}} \frac{1}{(2\pi)^2|\Lambda|^{1/2}} e^{-\frac{(\vec{x}-\vec{\mu})^H\Lambda^{-1}(\vec{x}-\vec{\mu})}{2}} d\vec{x}} \end{aligned} \quad (12)$$

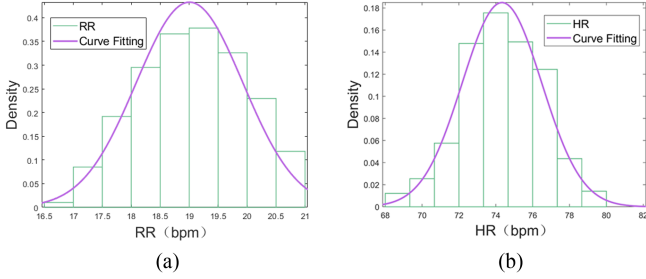


Fig. 4. FARH values follow normal distributions from extensive sampling. (a) Curve fitting of HR. (b) Curve fitting of RR.

$$\vec{x}_{\text{MAP}} = \arg \max_{\vec{x}} p(\vec{x}|y) \quad (13)$$

where $\vec{x} = [A_r, f_r, A_h, f_h]$ signifies the parameter vector, with $\vec{\mu} = [\mu_{A_r}, \mu_{f_r}, \mu_{A_h}, \mu_{f_h}]$ representing the mean values, $\Lambda = \text{diag}([\Lambda_{A_r}, \Lambda_{f_r}, \Lambda_{A_h}, \Lambda_{f_h}])$ indicating the diagonal matrix corresponding to the variances of \vec{x} , and σ^2 depicting the noise variance.

C. MEG Method

We use the posterior probability as the objective function within the FARH-defined solution space, optimizing it with the GWO. Nevertheless, the mean and variance of the FARH, as well as the variance of the noise—all of which directly affect the accuracy of estimation results—are unknown. Moreover, the maximum likelihood estimation cannot be employed to solve the hyperparameter since the joint probability density of the $S_c(\eta)$ and the FARH are the type II likelihood functions. To overcome these challenges, we apply the EM algorithm for iterative hyperparameter optimization. This process unfolds in the following manner.

By treating the vital sign parameters \vec{x} as latent variables, we aim to optimize

$$\begin{aligned} & E_{\vec{x}|y, \vec{\mu}, \Lambda, \sigma^2} [\log p(\vec{x}, y; \vec{\mu}, \Lambda, \sigma^2)] \\ &= E_{\vec{x}|y, \vec{\mu}, \Lambda, \sigma^2} [\log p(y|\vec{x}; \sigma^2) \cdot p(\vec{x}; \vec{\mu}, \Lambda)]. \end{aligned} \quad (14)$$

Here, the operation $E_{\vec{x}|y, \vec{\mu}, \Lambda, \sigma^2}[\cdot]$ represents an expectation relative to the distribution of \vec{x} , conditioned upon observed data and latent variables, denoting the posterior $p(\vec{x}|y, \vec{\mu}, \Lambda, \sigma^2)$.

Concerning A_r , by ignoring terms in the logarithm that do not depend on it, our objective becomes to optimize

$$E_{\vec{x}|y, \vec{\mu}, \Lambda, \sigma^2} [\log p(\vec{x}; \vec{\mu}, \Lambda)] \quad (15)$$

which, upon differentiation, leads to an update rule

$$\mu_{A_r}^k = A_r^k \quad (16)$$

where $\mu_{A_r}^{k+1} = E_{\vec{x}|y, \vec{\mu}^k, \Lambda^k, (\sigma^2)^k} (A_r)$. Similarly, we compute μ_{f_r} , μ_{A_h} , and μ_{f_h} .

For Λ_{A_r} , by similarly overlooking logarithm-independent terms, the objective is to maximize

$$E_{\vec{x}|y, \vec{\mu}, \Lambda, \sigma^2} [\log p(\vec{x}; \vec{\mu}, \Lambda)] \quad (17)$$

Algorithm 1: PSO Algorithm.

- 1: **Input:** Transmit signal parameters, r
- 2: **Output:** Optimal solution \vec{x}_{MAP}
- 3: **for** each particle i in the swarm **do**
- 4: Initialize velocity v_i and position \vec{x}_i of particle i
- 5: Evaluate the fitness of particle i and set $pBest_i = \vec{x}_i$
- 6: **end for**
- 7: Set $\vec{x}_{\text{MAP}} = \vec{x}_i(1, :)$; ▷ Initialize the global best solution
- 8: **while** termination criteria not met **do**
- 9: **for** $i = 1$ to N **do** ▷ Iterate over all particles
- 10: Update velocity v_i and position \vec{x}_i of particle i
- 11: Re-evaluate the fitness of particle i
- 12: **if** fitness of \vec{x}_i is better than $pBest_i$ **then**
- 13: Update $pBest_i = \vec{x}_i$
- 14: **end if**
- 15: **if** fitness of $pBest_i$ is better than the current global best **then**
- 16: Update global best $\vec{x}_{\text{MAP}} = pBest_i$
- 17: **end if**
- 18: **end for**
- 19: **end while**
- 20: **return** \vec{x}_{MAP} ▷ Return the optimal solution

which, following differentiation, updates as:

$$\Lambda_{A_r}^k = (A_r^k - \mu_{A_r}^k)^2 \quad (18)$$

where $\Lambda_{A_r}^{k+1} = E_{\vec{x}|y, \vec{\mu}^k, \Lambda^k, (\sigma^2)^k} \{(A_r - \mu_{A_r}^k)^2\}$. Proceeding similarly, we resolve Λ_{f_r} , Λ_{A_h} , and Λ_{f_h} .

Adopting a similar methodology for the noise parameter σ^2 , our goal is to maximize

$$E_{\vec{x}|y, \vec{\mu}, \Lambda, \sigma^2} [\log p(y|\vec{x}; \sigma^2)] \quad (19)$$

yielding

$$(\sigma^2)^{k+1} = E_{\vec{x}|y, \vec{\mu}^k, \Lambda^k, (\sigma^2)^k} (\|y - r\|^2 / N). \quad (20)$$

The EM algorithm has now resolved the mean and variance of the FARH, as well as the noise variance.

By applying the obtained hyperparameters to the model-solving process described above and using an optimization algorithm, specific FARH can be acquired. The PSO algorithm is suitable for this purpose [39]. The iterative nature of this procedure is elaborately described in Algorithm 1.

In addition to the traditional PSO algorithm, we have adopted the GWO to enhance our optimization process [40].

D. Enhanced Application of the GWO Algorithm for Vital Sign Detection

The GWO, inspired by the social structure and hunting strategies of grey wolves, uses a dynamic hierarchy of solutions— α , β , and γ —to efficiently explore and exploit the search space, significantly speeding up convergence and enhancing the detection accuracy of vital signs [41].

1) *Algorithmic Integration and Vital Sign Detection:* The hierarchical approach of the GWO is particularly suited for

Algorithm 2: GWO Algorithm for Vital Sign Detection.

- 1: **Input:** Transmit signal parameters, r
- 2: **Output:** Optimal solution \vec{x}_{MAP}
- 3: Initialize positions $\vec{\alpha}, \vec{\beta}, \vec{\gamma}, \vec{\omega}$ for the pack
- 4: Evaluate fitness of all wolves
- 5: Identify initial $\vec{\alpha}, \vec{\beta}, \vec{\gamma}$ based on the best fitness scores
- 6: **while** termination criteria not met **do**
- 7: **for** each wolf i in the pack **do**
- 8: Update the position of wolf i using:

$$\vec{x}_i^{t+1} = \vec{x}_i^t + \vec{A} \cdot (\vec{C} \cdot \vec{x}_p - \vec{x}_i^t)$$
- 9: Re-evaluate the fitness of wolf i
- 10: **if** fitness of \vec{x}_i is better **then**
- 11: Update $\vec{\alpha}, \vec{\beta}$, or $\vec{\gamma}$ if i is a better solution
- 12: **end if**
- 13: **end for**
- 14: Reduce \vec{a} \triangleright Decrease exploration, increase exploitation
- 15: **end while**
- 16: Set $\vec{x}_{\text{MAP}} = \vec{\alpha}$ \triangleright Alpha wolf holds the best solution
- 17: **return** \vec{x}_{MAP}

the dynamic and noisy environments typical in UWB radar signal processing. The algorithm assigns the best solution (α) to optimize the detection parameters for HR and HA, while the second-best solution (β) is optimized for detecting RR and RA, ensuring both vital signs are monitored with high accuracy.

2) *GWO Algorithm Process:*

- 1) *Initialization:* Positions of the wolves are initialized based on the transmit signal parameters.
- 2) *Fitness evaluation:* Each wolf's fitness is assessed based on its effectiveness in extracting HR and RR from the radar data.
- 3) *Leader updates and position adjustment:* Wolves update their positions using

$$\vec{x}_i^{t+1} = \vec{x}_i^t + \vec{A} \cdot (\vec{C} \cdot \vec{x}_p - \vec{x}_i^t)$$

where \vec{p} is selected from α , β , or γ , with coefficients \vec{A} and \vec{C}

$$\vec{A} = 2\vec{a} \cdot \vec{r}_1 - \vec{a}, \quad \vec{C} = 2 \cdot \vec{r}_2.$$

- 4) *Convergence check:* The process continues until termination criteria are met.
- 3) *Pseudocode:* The implementation details of the GWO algorithm used in our study are outlined in Algorithm 2.

Note that the application of different optimization algorithms could be further extended, but that is not the focus of this article.

IV. SIMULATION EXPERIMENT

A. Simulation Parameter Settings

A 120-s simulated monitoring experiment was conducted, utilizing the model described in Section II for the generation of vital signals. The parameters guiding the simulation are detailed in Table I.

TABLE I
SUMMARY OF KEY PARAMETERS

Parameters	Values
RR	[10, 25] bpm
HR	[65, 100] bpm
RA	[10, 15] mm
HA	[0.3, 0.7] mm
Center frequency	4.3 GHz
Bandwidth	1.7 GHz

TABLE II
COMPARATIVE ANALYSIS OF ESTIMATION ACCURACY FOR FARH

Method	RR(%)	HR(%)	RA(%)	HA(%)
Proposed	PSO 99.80	98.42	99.23	93.01
	GWO 99.87	98.68	99.44	95.06
CZT-MTI	97.15	95.12	-	-
MCM	97.15	91.39	-	-
VMD	98.22	88.63	-	-

The efficacy of our proposed framework is assessed against established benchmarks, including the CZT and moving target indicator (CZT-MTI) method [3], the multivariate correlation method (MCM) [23], and the VMD method [5]. We use the pre-set monitoring results as the baseline for comparative analysis.

The accuracy of FARH measurements over T seconds can be quantified as follows:

$$\text{Accuracy} = \frac{1}{T} \sum \left(1 - \frac{|r_{\text{est}} - r_{\text{ref}}|}{r_{\text{ref}}} \times 100\% \right). \quad (21)$$

Here, r_{est} denotes the frequency or amplitude estimated by our system, and r_{ref} represents the reference frequency or amplitude obtained from preset monitoring results or standard monitoring equipment. This equation provides an approach to evaluating the precision of vital sign estimation against established benchmarks.

B. Result Analysis

Table II presents a comparative analysis of FARH estimation accuracy within our experimental setup. It highlights the performance differences when the proposed framework employs the PSO and GWO algorithms, providing a clear evaluation of each optimization strategy's effectiveness.

Table II reveals that applying the GWO within the proposed framework further enhances accuracy. This improvement stems from GWO's advantages over the PSO. GWO demonstrates enhanced convergence capabilities, effectively avoiding local optima. By emulating the social hierarchy and hunting strategies of grey wolves, GWO achieves a balanced approach to exploration and exploitation, facilitating extensive initial searches and precise refinement in later stages. Moreover, GWO simplifies implementation with fewer parameter adjustments than PSO, enhancing its flexibility in accuracy estimation for VSS. This efficiency establishes GWO as a superior choice for VSS estimation. Notably, the proposed framework ultimately employs the GWO for enhanced accuracy.

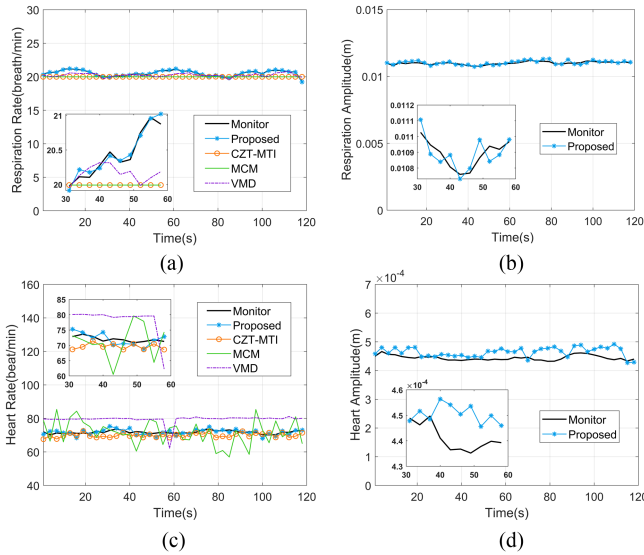


Fig. 5. Results of FARH estimate applying different methods with HSNR=0 dB. (a) RR. (b) RA. (c) HR. (d) HA.

Fig. 5 illustrates the results of FARH estimation using various methods, clearly presenting comparative findings.

For RR monitoring, the proposed framework achieves a superior accuracy of 99.87%, outperforming the CZT-MTI and MCM methods by 2.72%, and the VMD method by 1.65%. Regarding HR extraction, the proposed framework achieves an accuracy of 98.68%, outperforming the CZT-MTI method by 3.56%, the MCM method by 7.29%, and the VMD method by 10.05%.

The VMD method frequently misidentifies respiratory harmonics as HR when respiratory higher order harmonics overlap with the fundamental frequency of HR within the same frequency band. In RR monitoring, both the MCM and CZT-MTI methods select the peak frequency of the CZT spectrum as RR. However, the CZT-MTI method encounters a significant matter; as the HR band range often contains the fourth and fifth harmonics of respiration, suppressing respiratory harmonics also tends to suppress the heartbeat signal, making it difficult to detect HR effectively. The MCM is similarly limited; it relies on the harmonic of the heartbeat signal, so any absence or reduction of these components could skew the results. In addition, when RA are substantial, or noise levels are high, the above three methods are prone to incorrectly attributing intermodulation products or false peaks to HR. In contrast, the proposed framework begins by comprehensively utilizing vital sign information, followed by echo analysis to determine the FARH with the highest likelihood of occurrence. It avoids the impact of harmonics and intermodulation components on HR estimation.

In addition, the proposed framework demonstrates the precise recovery of RA and HA from echoes. Experimental results indicate that our framework achieves estimation accuracies of 99.44% for RA and 95.06% for HA, respectively.

C. Demonstration of Heartbeat Extraction Performance

To better assess the proposed framework's performance across various SNRs, we introduce a specialized metric, the heartbeat

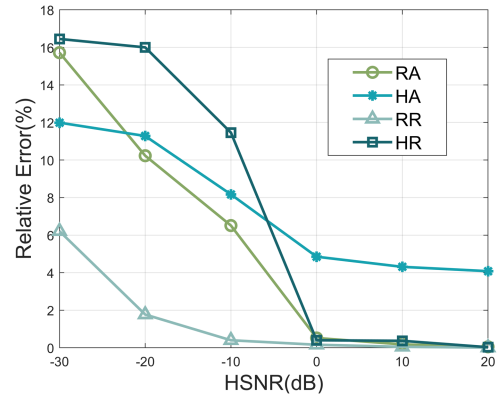


Fig. 6. Framework's antinoise performance in FARH extraction.

signal-to-noise ratio (HSNR). HSNR is mathematically defined as the decibel ratio of the heartbeat signal's power to the noise power, expressed as follows:

$$\text{HSNR} = 10 \log_{10} \left(\frac{P_{\text{heartbeat}}}{P_{\text{noise}}} \right). \quad (22)$$

This metric makes a more detailed assessment of the method's robustness in identifying HR through various noise levels.

Fig. 6 illustrates the antinoise performance of the proposed framework in extracting FARH. We use relative error as the measure for evaluation. Within the ranges listed in Table I, FARH values were randomly selected 200 times, respectively. As the HSNR increases, there is a significant decrease in the relative errors of the proposed framework. Since HSNR values in real situations mainly range from -10 to 5 dB, the proposed framework is expected to show high precision and strong robustness in real-world monitoring applications.

V. EXPERIMENTAL VALIDATION

A. Measurement Setup

In this experiment, we used the PulsOn 440, a typical IR-UWB monostatic radar module, as shown in Fig. 7(a). Fig. 7(b) illustrates the block diagram of the IR-UWB radar hardware system.

At the heart of this system, an IR-UWB pulse generator creates Gaussian pulses, which an onboard processor meticulously controls. These pulses are subsequently amplified by a power amplifier and emitted by the transmission antenna. The reception antenna captures the echoes, which are then processed through an analog-to-digital converter, filtering, and amplification by a low-noise amplifier, before being stored for analysis. The radar system facilitates the exchange of commands and data with the host PC via a universal serial bus connection. The time-domain waveform of the pulse transmitted by the P440 IR-UWB radar, as shown in Fig. 7(c), is centered at 4.3 GHz and exhibits a bandwidth of 2.2 GHz (an effective RF bandwidth of 1.4 GHz), as detailed in Fig. 7(e) [42]. Leveraging the coherent nature of UWB radar pulses, it is possible to integrate hundreds to thousands of pulses to significantly enhance the amplitude and SNR of the received signals, as detailed in [43].

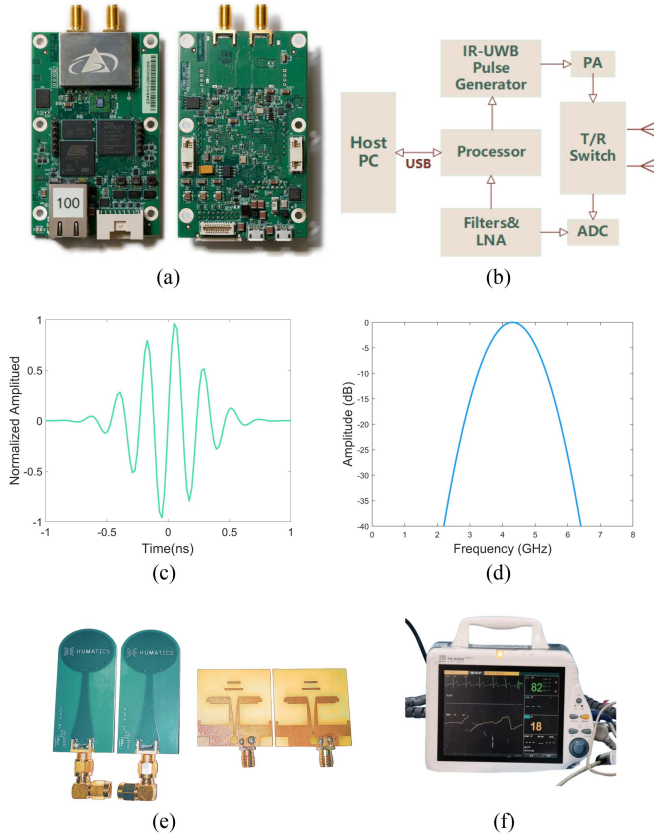


Fig. 7. (a) P440 IR-UWB radar. (b) Schematic representation of the IR-UWB radar operating principle. (c) Time domain of the transmitted waveform. (d) Frequency domain of the transmitted waveform. (e) Antennas utilized in the experiment: the antenna on the left-hand side is the original omnidirectional dipole model, while the antenna on the right-hand side is the improved broadband planar quasi-Yagi antenna. (f) Precision contact-based medical monitor provided by the hospital of the University of Electronic Science and Technology.

TABLE III
EXPERIMENTAL PARAMETERS FOR DATA COLLECTION

Experimental parameter	Value
IR-UWB bandwidth	2.2 GHz (3.1–5.3 GHz)
IR-UWB center frequency	4.3 GHz
Fast-time sampling period	61 ps
Slow-time repetition period	80 ms
Experimental distance	0.8 m
Monitoring duration	120 s

Table III lists the parameters used in the data collection. The sampling period T_f is 61 ps in fast-time processing, and the transmit pulse repetition period T_s is set to 0.08 s. The corresponding sampling frequency, $F_s = \frac{1}{T_s} = 12.5$ Hz, exceeds the Nyquist rate necessary for capturing both respiratory and heartbeat signals. Given the monitoring duration of 120 s, as illustrated in Fig. 2, the number of slow-time samples totals 1500.

To reduce the coupling noise in echoes, we revised our deployment strategy to use improved broadband planar quasi-Yagi antennas, replacing the original omnidirectional dipole antennas, as illustrated in Fig. 7(e). These new antennas maintain a group

TABLE IV
TECHNICAL PARAMETERS OF THE IMPROVED BROADBAND PLANAR QUASI-YAGI ANTENNAS

Parameters	Values
Working Band	2.9–10.1 GHz
Polarization Mode	Linear polarized
Group Delay	< 0.82 ns
Efficiency	Usually >90%, Minimum >71%
Gain	5–7 dB

delay of no more than 0.82 ns and offer significant directivity across a wide frequency range. The key characteristics of the antenna are detailed in Table IV.

B. Experimental Scenario

To validate the experiment, we selected two volunteers, a female and a male, both aged between 20 and 30. Fig. 8 shows the experimental setup, where the volunteers' orientations were adjusted relative to the radar, with each volunteer tested from eight different angles. The volunteers and the antenna were kept at a fixed distance of 0.8 m. For comparison, we used a precision contact-based medical monitor as a benchmark, as shown in Fig. 7(f).

However, due to technological limitations, current contact monitoring devices cannot measure the amplitude of vital signs. Consequently, our experiments will exclude the demonstration of monitoring results and accuracy comparisons for the amplitude information of vital signs.

C. Onsite Experimental Results

The estimations of RR and HR are conducted over 120 s, utilizing a sliding window of 10 s that overlaps by 8 s in each subsequent measurement throughout the experiments. Given the limitations on page length, Fig. 9 illustrates the continuous measurement results over 120 s in one orientation, representing each volunteer. Table V outlines the comparative accuracy of estimating RR and HR under varying body orientations.

D. Result Analysis

As given in Table V, we evaluated the detection performance of the proposed framework at various azimuth angles by adjusting the volunteer's orientation relative to the radar. The results show that the performance of all three methods declines noticeably with changes in θ , primarily due to a decrease in the effective reflective area as the human body moves away from the radar. For example, as the azimuth angle increases from 0° to 90° , the SNR of the echo decreases, resulting in higher estimation errors. Nevertheless, the proposed framework consistently outperforms other methods, demonstrating robustness to changes in body orientation with its superior vital sign extraction capabilities, as detailed in Section III.

In the onsite experiments, the proposed framework achieves an average HR accuracy of 93.57%, which is 6.34% higher than that of the MCM. Notably, the MCM was previously the

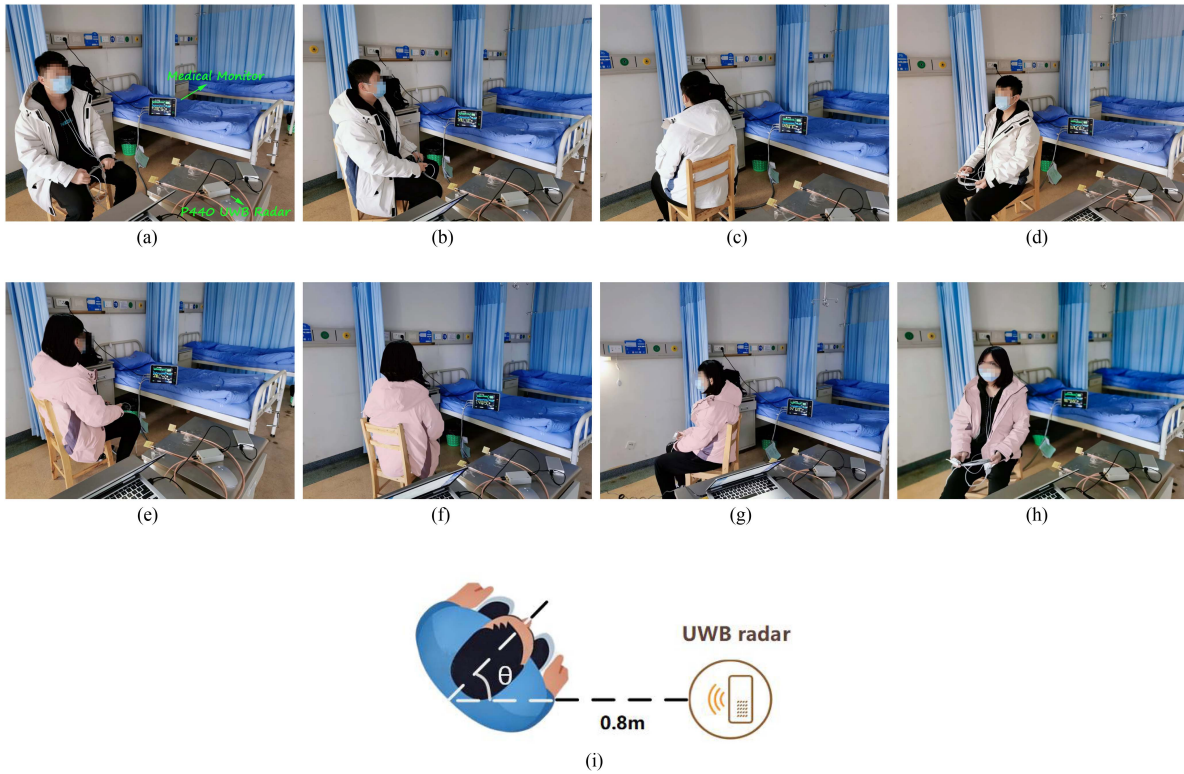


Fig. 8. Experimental scenario in different body orientations. (a) $\theta = 0^\circ$ of volunteer 1. (b) $\theta = 45^\circ$ of volunteer 1. (c) $\theta = 180^\circ$ of volunteer 1. (d) $\theta = 270^\circ$ of volunteer 1. (e) $\theta = 90^\circ$ of volunteer 2. (f) $\theta = 135^\circ$ of volunteer 2. (g) $\theta = 225^\circ$ of volunteer 2. (h) $\theta = 315^\circ$ of volunteer 2. (i) Schematic representation of the experimental scenarios at various angles.

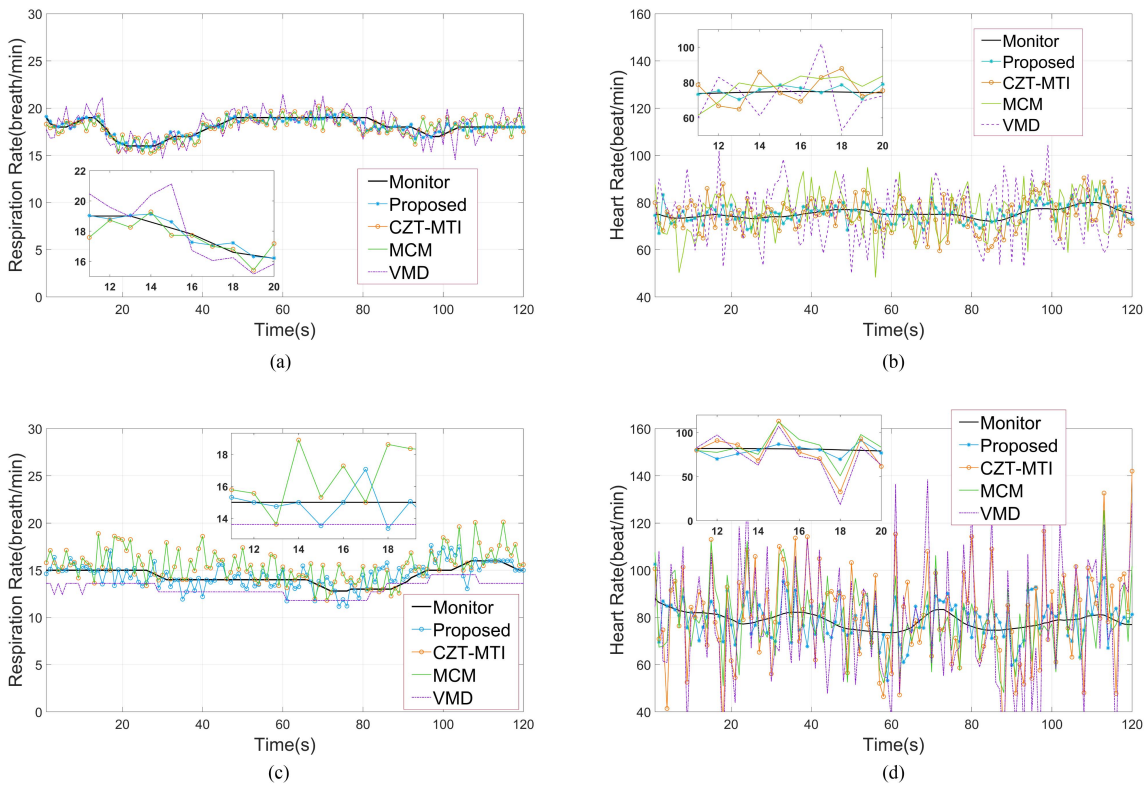


Fig. 9. RR and HR estimation results from various methods. (a) RR of volunteer 1 at 0° . (b) HR of volunteer 1 at 0° . (c) RR of volunteer 2 at 90° . (d) HR of volunteer 2 at 90° .

TABLE V
RR AND HR ACCURACY AMONG DIFFERENT METHODS

	RR (%)				HR (%)				
	CZT-MTI	MCM	VMD	Pro.	CZT-MTI	MCM	VMD	Pro.	
volunteer 1	0°	96.98	96.98	95.03	98.91	92.88	90.27	86.74	96.99
	45°	93.72	93.72	92.33	96.56	87.12	87.03	79.19	94.17
	90°	90.65	90.65	90.73	94.31	80.72	84.69	75.03	91.55
	135°	92.14	92.14	91.35	95.02	85.55	86.74	80.68	92.87
	180°	94.53	94.53	93.35	96.04	89.27	88.79	83.06	94.86
	225°	92.13	92.13	91.33	95.11	85.13	86.65	82.74	92.83
	270°	90.72	90.72	90.90	94.51	79.12	85.14	74.63	91.71
	315°	93.33	93.33	91.96	95.83	86.08	87.96	80.20	94.53
	Avg.	93.03	93.03	92.12	95.78	85.73	87.16	80.28	93.69
volunteer 2	0°	97.06	97.06	96.86	99.01	92.53	89.52	86.40	96.13
	45°	93.98	93.98	92.45	96.61	87.03	88.21	78.12	94.64
	90°	90.08	90.08	90.79	94.23	79.62	85.49	73.68	91.69
	135°	92.70	92.70	91.92	95.28	84.79	86.40	80.25	92.27
	180°	95.00	95.00	93.74	96.49	88.80	88.90	84.10	94.76
	225°	91.81	91.81	91.00	94.52	83.54	86.87	81.00	92.89
	270°	90.71	90.71	90.48	94.78	77.19	85.67	77.58	91.20
	315°	93.62	93.62	91.73	96.32	88.70	87.54	81.81	93.98
	Avg.	93.12	93.12	92.37	95.89	85.28	87.33	80.37	93.45

The bold values are intended to highlight the results derived from our proposed methods.

most accurate among the three existing methods examined. The proposed framework extracts RR with an average accuracy of 95.84%, marking a 2.76% improvement over the CZT-MTI and MCM methods. Furthermore, it surpasses the VMD method by an increase of 3.09%. Given the relatively large amplitude of respiratory motions across various directions of the human body, this characteristic alone does not demonstrate the distinct advantage of the proposed framework. Therefore, our framework's superiority is highlighted by its ability to detect weak HR across various body orientations.

Further analysis of other aspects has been discussed in Section IV-B, and the experimental results corroborate the findings from the simulations.

VI. CONCLUSION

In this work, we propose a groundbreaking framework for vital sign estimation using the IR-UWB system. Designed to identify reliable VSS, our algorithm is both rational and coherent. The framework significantly enhances robustness against noise. In addition, it offers improved adaptability over conventional methods, which primarily focus on frontal chest monitoring. It also facilitates the accurate extraction of FARH from a probabilistic perspective without relying on prior knowledge. Compared to CZT-MTI, VMD, and MCM, our framework demonstrates superior estimation accuracy in onsite experiments. Remarkably, it achieves an average HR accuracy of 93.57%, which is 6.34% higher than that of the MCM—the best-performing benchmark. Furthermore, it excels in amplitude data extraction with over 95% accuracy, surpassing the capabilities of existing methods.

Looking ahead, we plan to enhance the framework's capabilities by integrating multiple sensors and refining our algorithms

to monitor individuals in motion and simultaneously handle multiple targets. This expansion will leverage advancements in signal processing and machine learning, aiming to transform noncontact monitoring technologies for broader application in dynamic environments, thus pushing the boundaries of remote health monitoring.

REFERENCES

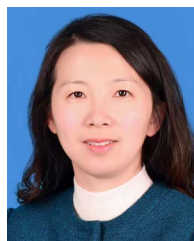
- [1] G. Paterniani et al., "Radar-based monitoring of vital signs: A tutorial overview," *Proc. IEEE*, vol. 111, no. 3, pp. 277–317, Mar. 2023.
- [2] F. Jing, J. Liang, Y. Wang, and P. Chen, "Harmonics and intermodulation products-based fuzzy logic (HIPBFL) algorithm for vital sign frequency estimation using a UWB radar," *Expert Syst. Appl.*, vol. 228, 2023, Art. no. 120294.
- [3] A. Lazaro, D. Girbau, and R. Villarino, "Analysis of vital signs monitoring using an IR-UWB radar," *Prog. Electromagnetics Res.*, vol. 100, pp. 265–284, 2010.
- [4] J. Li, L. Liu, Z. Zeng, and F. Liu, "Advanced signal processing for vital sign extraction with applications in UWB radar detection of trapped victims in complex environments," *IEEE J. Sel. Topics Appl. Earth Observ. Remote Sens.*, vol. 7, no. 3, pp. 783–791, Mar. 2014.
- [5] Z. Duan and J. Liang, "Non-contact detection of vital signs using a UWB radar sensor," *IEEE Access*, vol. 7, pp. 36888–36895, 2019.
- [6] Y. Zhang, R. Yang, Y. Yue, E. G. Lim, and Z. Wang, "An overview of algorithms for contactless cardiac feature extraction from radar signals: Advances and challenges," *IEEE Trans. Instrum. Meas.*, vol. 72, Aug. 2023, Art. no. 4009520.
- [7] T. Pan, Y. Guo, W. Guo, and C. Kang, "Detection of vital sign based on UWB radar by a time domain coherent accumulation method," *IEEE Sens. J.*, vol. 23, no. 15, pp. 17054–17063, Aug. 2023.
- [8] S. Wu et al., "Study on a novel UWB linear array human respiration model and detection method," *IEEE J. Sel. Topics Appl. Earth Observ. Remote Sens.*, vol. 9, no. 1, pp. 125–140, Jan. 2016.
- [9] B. P. A. Rohman, M. B. Andra, and M. Nishimoto, "Through-the-wall human respiration detection using UWB impulse radar on hovering drone," *IEEE J. Sel. Topics Appl. Earth Observ. Remote Sens.*, vol. 14, pp. 6572–6584, Jun. 2021.
- [10] L. Qiao et al., "Spectral unmixing successive variational mode decomposition for robust vital signs detection using UWB radar," *IEEE Trans. Instrum. Meas.*, vol. 72, May 2023, Art. no. 8502813.

- [11] C. G. Bilich, "Bio-medical sensing using ultra wideband communications and radar technology: A feasibility study," in *Proc. Pervasive Health Conf. Workshops*, Innsbruck, Austria, 2006, pp. 1–9.
- [12] A. Lazaro, D. Girbau, and R. Villarino, "Techniques for clutter suppression in the presence of body movements during the detection of respiratory activity through UWB radars," *Sensors*, vol. 14, no. 2, pp. 2595–2618, 2014.
- [13] Y. Rong, A. R. Chiriyath, A. Dutta, and D. W. Bliss, "Active breathing suppression for improved sleep monitoring heartbeat detection using UWB radar," in *Proc. IEEE 8th Int. Workshop Comput. Adv. Multi-Sensor Adaptive Process.*, Le Gosier, Guadeloupe, 2019, pp. 161–165.
- [14] E. Schires, P. Georgiou, and T. S. Lande, "Vital sign monitoring through the back using an UWB impulse radar with body coupled antennas," *IEEE Trans. Biomed. Circuits Syst.*, vol. 12, no. 2, pp. 292–302, Apr. 2018.
- [15] K.-K. Shyu, L.-J. Chiu, P.-L. Lee, and L.-H. Lee, "UWB simultaneous breathing and heart rate detections in driving scenario using multi-feature alignment two-layer EEMD method," *IEEE Sens. J.*, vol. 20, no. 17, pp. 10251–10266, Sep. 2020.
- [16] S. Lim, S. Lee, J. Jung, and S.-C. Kim, "Detection and localization of people inside vehicle using impulse radio ultra-wideband radar sensor," *IEEE Sens. J.*, vol. 20, no. 7, pp. 3892–3901, Apr. 2020.
- [17] X. Yang, Y. Ding, X. Zhang, and L. Zhang, "Spatial-temporal-Circulated GLCM and physiological features for in-vehicle people sensing based on IR-UWB radar," *IEEE Trans. Instrum. Meas.*, vol. 71, Apr. 2022, Art. no. 8502113.
- [18] A. Sarkar and D. Ghosh, "Accurate sensing of multiple humans buried under rubble using IR-UWB SISO radar during search and rescue," *Sens. Actuators A: Phys.*, vol. 348, 2022, Art. no. 113975.
- [19] M. Le, "Heartbeat extraction based on a high order derivative for ultra-wideband impulse radar application," *J. Phys. D, Appl. Phys.*, vol. 53, no. 18, 2020, Art. no. 18LT02.
- [20] S. Wang et al., "Radar cardiogram extraction and respiratory harmonic suppression based on optimized feedback notch filters," *IEEE Access*, vol. 12, pp. 32298–32307, 2024.
- [21] Y. Xiong, S. Chen, X. Dong, Z. Peng, and W. Zhang, "Accurate measurement in Doppler radar vital sign detection based on parameterized demodulation," *IEEE Trans. Microw. Theory Techn.*, vol. 65, no. 11, pp. 4483–4492, Nov. 2017.
- [22] V. Nguyen, A. Q. Javaid, and M. A. Weitnauer, "Harmonic path (HAPA) algorithm for non-contact vital signs monitoring with IR-UWB radar," in *Proc. IEEE Biomed. Circuits Syst. Conf.*, Rotterdam, The Netherlands, 2013, pp. 146–149.
- [23] M. Le and B. V. Nguyen, "Multivariate correlation of higher harmonics for heart rate remote measurement using UWB impulse radar," *IEEE Sens. J.*, vol. 20, no. 4, pp. 1859–1866, Feb. 2020.
- [24] H. Shen et al., "Respiration and heartbeat rates measurement based on autocorrelation using IR-UWB radar," *IEEE Trans. Circuits Syst. II Exp. Briefs*, vol. 65, no. 10, pp. 1470–1474, Oct. 2018.
- [25] K. J. Lee, C. Park, and B. Lee, "Tracking driver's heart rate by continuous-wave Doppler radar," in *Proc. IEEE Annu. Int. Conf. IEEE Eng. Med. Biol. Soc.*, Orlando, FL, USA, 2016, pp. 5417–5420.
- [26] K. Dragomiretskiy and D. Zosso, "Variational mode decomposition," *IEEE Trans. Signal Process.*, vol. 62, no. 3, pp. 531–544, Feb. 2014.
- [27] C. Ye and T. Ohtsuki, "Spectral Viterbi algorithm for contactless wide-range heart rate estimation with deep clustering," *IEEE Trans. Microw. Theory Techn.*, vol. 69, no. 5, pp. 2629–2641, May 2021.
- [28] C. Ding, J. Yan, L. Zhang, H. Zhao, H. Hong, and X. Zhu, "Noncontact multiple targets vital sign detection based on VMD algorithm," in *Proc. IEEE Radar Conf.*, Seattle, WA, USA, 2017, pp. 0727–0730.
- [29] Y. Rong and D. W. Bliss, "Remote sensing for vital information based on spectral-domain harmonic signatures," *IEEE Trans. Aerosp. Electron. Syst.*, vol. 55, no. 6, pp. 3454–3465, Dec. 2019.
- [30] P. Bechet, R. Mitran, and M. Munteanu, "A non-contact method based on multiple signal classification algorithm to reduce the measurement time for accurately heart rate detection," *Rev. Sci. Instrum.*, vol. 84, no. 8, Aug. 2013, Art. no. 084707.
- [31] K. Yamamoto, K. Toyoda, and T. Ohtsuki, "Non-contact heartbeat detection by MUSIC with discrete cosine transform-based parameter adjustment," in *Proc. IEEE Glob. Commun. Conf.*, Abu Dhabi, United Arab Emirates, Dec. 2018, pp. 1–6.
- [32] X. Liang, H. Zhang, S. Ye, G. Fang, and T. A. Gulliver, "Improved denoising method for through-wall vital sign detection using UWB impulse radar," *Digit. Signal Process.*, vol. 74, pp. 72–93, Mar. 2018.
- [33] L. Sun et al., "Remote measurement of human vital signs based on joint-range adaptive EEMD," *IEEE Access*, vol. 8, pp. 68514–68524, 2020.
- [34] J. Zhang, Y. Wu, Y. Chen, and T. Chen, "Health-radio: Towards contactless myocardial infarction detection using radio signals," *IEEE Trans. Mobile Comput.*, vol. 21, no. 2, pp. 585–597, Feb. 2022.
- [35] X. Zhang, Z. Liu, Y. Kong, and C. Li, "Mutual interference suppression using signal separation and adaptive mode decomposition in noncontact vital sign measurements," *IEEE Trans. Instrum. Meas.*, vol. 71, Mar. 2022, Art. no. 4001015.
- [36] L. Qu, C. Liu, T. Yang, and Y. Sun, "Vital sign detection of FMCW radar based on improved adaptive parameter variational mode decomposition," *IEEE Sens. J.*, vol. 23, no. 20, pp. 25048–25060, Oct. 2023.
- [37] Q. Zhai, X. Han, Y. Han, J. Yi, S. Wang, and T. Liu, "A contactless on-bed radar system for human respiration monitoring," *IEEE Trans. Instrum. Meas.*, vol. 71, Apr. 2022, Art. no. 4004210.
- [38] C. Li and J. Lin, "Random body movement cancellation in Doppler radar vital sign detection," *IEEE Trans. Microw. Theory Techn.*, vol. 56, no. 12, pp. 3143–3152, Dec. 2008.
- [39] J. Kennedy and R. Eberhart, "Particle swarm optimization," in *Proc. ICNN'95: Int. Conf. Neural Netw.*, Perth, WA, Australia, 1995, pp. 1942–1948.
- [40] S. Mirjalili, S. M. Mirjalili, and A. Lewis, "Grey wolf optimizer," *Adv. Eng. Softw.*, vol. 69, pp. 46–41, 2014.
- [41] T. Pardhu and V. Kumar, "Human motion classification using impulse radio ultra wide band through-wall RADAR model," *Multimedia Tools Appl.*, vol. 82, no. 24, pp. 36769–36791, 2023.
- [42] *Time Domains Ultrawide Band (UWB): Definition and Advantages*, Time Domain Company, Waltham, MA, USA, 2012.
- [43] *Monostatic Radar Module Reconfiguration and Evaluation Tool (MRM RET) User Guide*, Time Domain Company, Waltham, MA, USA, 2014.



Yizhu Wang (Student Member, IEEE) received the B.S. degree in electronic information engineering in 2022 from the University of Electronic Science and Technology of China, Chengdu, China, where she is currently working toward the master's degree in information and communication engineering with the School of Information and Communication Engineering.

Her research interests include radar signal processing and vital signs extraction.



Jing Liang (Senior Member, IEEE) received the B.S. and M.Sc. degrees in electrical engineering from the Beijing University of Posts and Telecommunications, Beijing, China, in 2003 and 2006, respectively, and the Ph.D. degree in electrical engineering from The University of Texas at Arlington, Arlington, TX, USA, in 2009.

She is currently a Professor with the School of Information and Communication Engineering, University of Electronic Science and Technology of China, Chengdu, China. Her research interests include radar sensor networks, collaborative and distributed signal processing, wireless communication networks, fuzzy logic, and machine learning.

Dr. Liang is currently a TPC co-chair for several international conferences. She was a Guest Editor for IEEE Internet of Things Journal, *Pattern Recognition (Elsevier)*, and *IEEE Network*. She was the recipient of the Hundred Talent Plan, Sichuan, China, and was the Key Project Leader of the National Natural Science Foundation of China.